

# Model-based Deep Learning and Monotone Operator Learning for Quantitative Susceptibility Mapping

Kajan Subakannan

Department of Biomedical Engineering and Medical Physics  
University College London

## Abstract

Quantitative susceptibility mapping (QSM) is a novel MRI technique for mapping magnetic susceptibility distributions in biological tissues, enabling improved microstructure distinguishment in images. This recently developed technique, whilst effective, does come with some technical challenges. One stage of the QSM pipeline is called the dipole inversion, which involves a deconvolution problem that is ill-posed, making it difficult to compute conventionally. Traditional QSM methods rely on iterative unrolled algorithm approaches, which are computationally intensive and memory inefficient. In this paper, we present an alternative approach using model-based deep learning and monotone operator learning for QSM reconstruction, which proves to be capable of reconstructing 3D MRI QSM images more accurately than traditional methods, whilst remaining memory efficient.

## Table of Contents

Model-based Deep Learning and Monotone Operator Learning for Quantitative Susceptibility Mapping .....	2
1. INTRODUCTION .....	4
1.1 Magnetic Resonance Imaging .....	4
1.2 Quantitative Susceptibility Mapping .....	4
1.3 The QSM Pipeline .....	5
1.4 Dipole Inversion .....	6
1.5 Research Objective .....	6
2. BACKGROUND .....	7
2.1 The QSM Challenge .....	7
2.2 k-space Methods .....	7
2.3 The proposed solution .....	7
2.4 Monotone Operator Learning & Model-Based Deep Learning .....	8
2.4.1 Monotone Operator Learning Breakdown .....	8
2.4.2 Implementation Variants – Spectral Normalisation and Lipschitz Regularisation .....	9
2.4.3 Supervised Training .....	10
2.4.4 Performance of MOL-SN and MOL-LR against Unrolled Algorithms .....	10
2.4.5 Review of MOL Literature .....	10
3. METHODOLOGY .....	12
3.1 Justification of Fundamentals .....	12

3.2 The Forward and Adjoint Operators .....	12
3.3 2D Convolution and Deconvolution .....	13
3.4 2D to 3D Framework Modification .....	13
3.5 Visualising and Implementing the Dipole .....	14
3.6 3D Dipole Inversion.....	14
3.7 Hyperparameter Tuning .....	14
3.8 Multiple Batch Model Training .....	16
3.9 3D Large Brain Image Susceptibility Map Reconstruction .....	16
3.10 Methodology Summary .....	16
4. RESULTS AND ANALYSIS .....	17
4.1 2D SENSE vs MOL .....	17
4.2 3D SENSE vs MOL: Simple Sphere .....	17
4.3 3D SENSE vs MOL: Simulated Phase (Training, Non-comparative).....	18
4.4 3D SENSE vs MOL: Brain Image QSM Reconstruction .....	19
5. DISCUSSION .....	22
6. CONCLUSION.....	22

## 1. INTRODUCTION

### 1.1 Magnetic Resonance Imaging

Magnetic Resonance Imaging (MRI) is one of the most powerful medical imaging techniques currently available for clinical use. It enables the non-invasive visualisation of internal anatomical structures, producing high-detail three-dimensional images, and is typically used to assist with obtaining diagnoses, monitoring treatments, and detecting diseases [1]. MRIs excel in producing higher resolution images, soft tissue images, and are unique compared to other imaging techniques such as X-rays and CT scans in that they don't use any radiation [2]. MRIs function by producing a strong magnetic field via powerful magnets, resulting in the protons of the hydrogen atoms in the tissue aligning their axes with the field. A radiofrequency current is then directed at the aligned hydrogen atoms, causing them to absorb this energy, causing them to rotate out of their original alignment. The radiofrequency current is then turned off, and as the hydrogen atoms gradually return to their original alignment with the magnetic field, they emit the absorbed energy in the form of radio waves. The time taken for the hydrogen atoms to return to their original alignment is known as the 'relaxation time', and it varies between different types of tissue[3]. The MRI machine has coils that detect the emitted radio waves and process them using complex algorithms to construct three-dimensional images of the body. Since different tissues within the body have different relaxation times, the images can also differentiate between various types of tissue, such as muscle, fat and organs.

This method of tissue differentiation does however not provide sufficient sensitivity to subtle changes in tissue microstructure, such as alterations in myelin content or neuronal integrity. Traditional MRIs similarly struggle to detect differentiation between tissues with similar signal intensities or relaxation times. This is a key shortcoming of MRIs, as there are a plethora of conditions that rely on being able to distinguish between tissues and other substances with similar signal intensities, especially in complex organs like the brain. Examples of conditions that MRIs struggle with include haemorrhages and lesions. Distinguishing between different types of haemorrhages (e.g. acute versus chronic) and being able to discern them from the surrounding tissue can be very challenging for traditional MRIs but is crucial information for guiding treatment decisions and predicting patient outcomes. Traditional MRIs may also struggle with characterising lesions due to them exhibiting similar signal intensities. There are a multitude of brain lesions, ranging from cysts to glioblastomas to brain tumours, and identifying the lesions incorrectly can have devastating consequences.

MRIs also lack the sensitivity to detect and quantify iron depositions in the brain. Iron accumulation in the brain has been proven to be associated with neurodegenerative disorders like Parkinson's disease and Alzheimer's disease [5][6]. The inability to detect and distinguish these microstructural nuances can be detrimental to patient health and well-being as a result of ineffective treatment planning or misdiagnosis'.

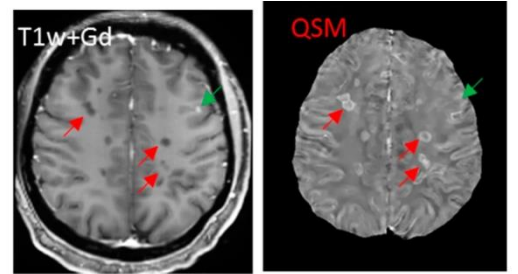


Figure 1 - Lesions in T1 weighted MRI image vs QSM. In the lesions in the QSM image, both hypointense and hyper intense parts of the lesion are visible. Hyperintense rings are an indication of conditions such as Parkinson's. [4]

### 1.2 Quantitative Susceptibility Mapping

Quantitative Susceptibility Mapping (QSM) is a recently developed advanced MRI technique, that measures and maps the spatial magnetic susceptibility distribution within biological tissues, as opposed to just the magnitude of the signals detected by the coils.

Magnetic Susceptibility is a fundamental property of any material or tissue, and it dictates the materials' response to an applied external magnetic field [7]. It provides insight into the tissue composition and microstructure by being able to visualise both positive and negative susceptibility values. Positive susceptibility values indicate paramagnetic behaviour, meaning that the tissue enhances the magnetisation in the presence of an applied magnetic field. In contrast, negative susceptibility values signify diamagnetic properties, where tissues reduce the magnetisation in the presence of an applied magnetic field.

The susceptibility of a material is determined by the interaction of magnetic fields with the electronic configuration of atoms and molecules within it, with factors influencing it including the number of unpaired electrons, orbital motions and chemical bonding within the different parts of the tissue. The manner in which the different tissue constituents contribute to the overall susceptibility of the tissue can be described by Wiedemann's Additivity Law, which states that the overall magnetic susceptibility of a mixture is the weighted sum of the magnetic susceptibility of its constituents, weighted according to their relative volumes of occupation of the mixture[8][29]. This can be expressed mathematically as

$$\chi_{volume} = \frac{\sum_{i=1}^N V_i \chi_i}{\sum_{i=1}^N V_i}$$

where  $V_i$  represents the volume of the tissue occupied by substance  $i$ , which has a magnetic susceptibility  $\chi_i$ .

What makes QSM an extension of traditional MRI is that its data acquisition method is the same as a typical MRI, or more specifically  $T_2^*$ -weighted gradient echo MRI sequences, and the QSM technique lies in the post-processing of the raw data retrieved by the MRI coils. An MRI signal consists of 2 main components, magnitude and phase, due to the MRI signal being complex. The magnitude component provides information about tissue density and proton concentration and is what is visualised in traditional MR images. The phase component of  $T_2^*$ -weighted gradient echo MRI sequences reflects the local magnetic field perturbations, which are induced by the tissue susceptibility variations. The relationship between the phase  $\phi$  and the magnetic field perturbation  $\Delta B_z$ , is expressed linearly as:

$$\phi(r) = \gamma \cdot TE \cdot \Delta B_z(r) + \phi_0(r)$$

where  $\gamma$  is the gyromagnetic ratio, TE is the echo time,  $r$  is the distance from each point or voxel on the map and  $\phi_0(r)$  represents the phase at TE=0 [7].

### 1.3 The QSM Pipeline

The process of obtaining a map of the magnetic field perturbation, and then the susceptibility map  $\chi$ , from the phase is known as the QSM pipeline.

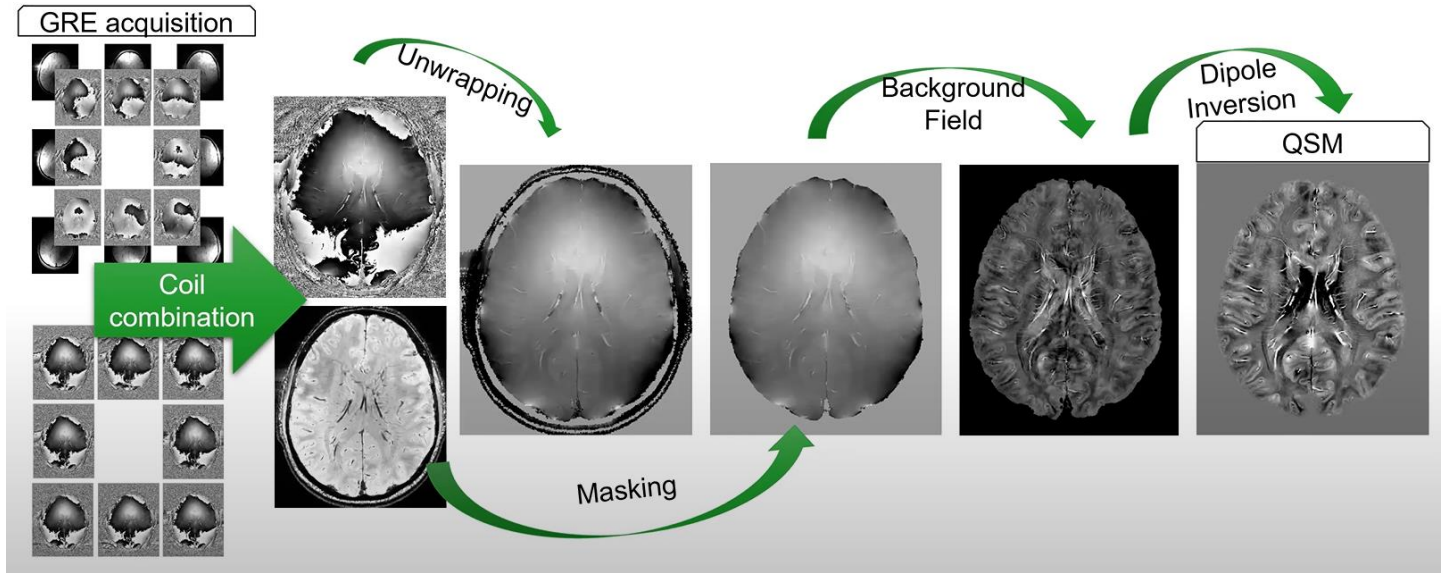


Figure 2 - QSM Pipeline [9]

The QSM pipeline starts with the acquisition of the complex  $T_2^*$ -weighted gradient echo MRI sequences, from which the phase images are extracted. Phase fitting takes place during this stage, which removes phase offsets & enhances susceptibility-related phase contrast [10].

Secondly, the phase is unwrapped. Phase images are prone to phase wrapping, where phase values ‘wrap-around’ from 0 to  $2\pi$ . Phase unwrapping algorithms are employed to correct the phase wraps and ensure continuity in the phase values throughout the image. A map of the magnetic field perturbation is then computed, however, it still requires some more processing before it is sufficient.

Next is Background Field Removal. The susceptibility differences between the desired tissue and the surrounding non-tissue regions such as air cause undesired field variations. The most common technique for removing these background fields is projecting the image onto dipole fields, which model and subtract the background fields.

Following this, the processed phase is used to produce the susceptibility-induced field perturbation map.

The penultimate stage of the QSM pipeline is masking and noise reduction, which remove data from regions with no MRI signal, to improve the accuracy of subsequent processing steps. The result after this is a masked magnetic field perturbation map with no background field. At this point, the magnetic field perturbation map has been sufficiently processed and can be used to obtain the magnetic susceptibility map [8]. The relationship between the field perturbation and susceptibility is illustrated by:

$$\Delta B_z(r) = B_0 \cdot d(r) * \chi(r)$$

This shows that the magnetic field perturbation is equal to the convolution of the susceptibility and a unit magnetic dipole within a magnetic field  $B_0$ . Obtaining the field perturbations from a known susceptibility and dipole kernel is known as the forward problem, and is fairly straightforward. However, in the QSM pipeline, the susceptibility is the unknown. This outlines the final stage of the QSM pipeline, whereby the inverse problem must be solved. This is referred to as dipole inversion.

### 1.4 Dipole Inversion

The dipole kernel describes the magnetic field perturbations produced by a point-like magnetic susceptibility source, within a homogeneous magnetic field  $B_0$  that is along the z-direction [10]. It has a characteristic dipolar spatial distribution, and is mathematically expressed as

$$d(r) = \frac{3 \cos^2 \theta - 1}{4\pi r^4}$$

Finding the susceptibility from the field perturbation map and the dipole kernel, i.e. the process of dipole inversion, involves deconvolution using the dipole kernel. Due to its dipolar nature, at  $54.7^\circ$  relative to the magnetic field  $B_0$ , the kernel value is zero. This is an expected property of dipoles since it must be 0 at some angle since the polarity changes. Because of this property, deconvolution becomes an ill-posed, ill-conditioned inverse problem, meaning the solution lacks a unique solution, and the solutions are highly sensitive to small changes in the inputs. The dipole inversion process is also incredibly computationally demanding, hence why QSM images are 2-dimensional. Reconstructing 3-dimensional, high-resolution images with reasonable accuracy would require high-performance computers and would have to be allowed to reconstruct the image over a long period of time, which is entirely too inefficient to be considered for clinical applications. This is also a large hindrance since being able to visualise MRI images in 3D aids

doctors, clinicians, and diagnosticians immensely, and improves patient outcomes. These factors are where the difficulties in QSM lie.

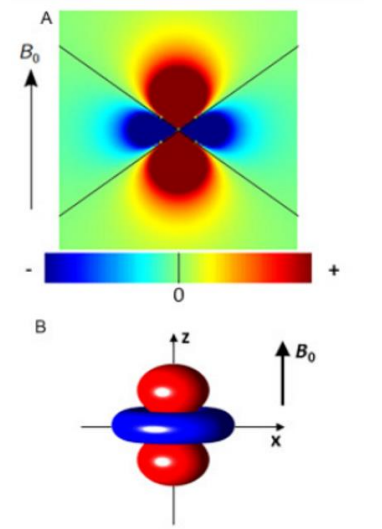


Figure 3 –

A. 2D slice through dipole kernel along XZ plane.

B. 3D visualisation of shape of dipole kernel [8]

### 1.5 Research Objective

The main aim of this project is to develop a method for accurately and efficiently reconstructing magnetic susceptibility maps in 3D from 3D magnetic field perturbation map inputs. The devised method will utilise memory-efficient model-based deep learning. The method will be tested on 2D and 3D images, as well as 3D brain images, whilst being compared to a traditional algorithm, in order to ascertain clinical viability and improvement on current practices. Then, the model's hyperparameters will be optimised to produce the most accurate results.

## 2. BACKGROUND

Tackling the ill-posed, ill-conditioned dipole inversion problem is a key challenge in the QSM community. There are a variety of different approaches that can be used, but the consensus on the approaches used is that, mathematically, the inversion involves solving a minimisation problem with a data fidelity term and a regularisation term. The data fidelity term measures the difference between the estimated tissue fields, and the regularisation term incorporates additional information about the unknown susceptibility map to suppress artefacts in the solution. The minimisation problem is solved iteratively, with the regularisation strength  $\lambda$  being optimised to balance the artefact suppression and image sharpness.[8]

### 2.1 The QSM Challenge

In 2016, the QSM community organised the QSM challenge, aimed at quantitatively assessing the performance of different QSM algorithms' ability to accurately reconstruct the magnetic susceptibility distribution from phase images.[12] Participants were provided with  $T_2^*$ -weighted gradient echo MR phase images of a healthy volunteer's brain, and the algorithms developed were comparatively analysed, allowing researchers to identify strengths, weaknesses and areas for improvement in existing techniques. Prior to the challenge, image-space-based regularisation methods were the convention, focusing on an optimisation approach for the minimisation problem, which is described by:

$$\chi(r) = \operatorname{argmin}_{\chi(r)} \|w(\Delta B_z(r) - d(r) * \chi(r))\|_2^2 + \lambda R(\chi)$$

This approach tries to find the value that  $\chi(r)$  can take such that  $\|w(\Delta B_z(r) - d(r) * \chi(r))\|_2^2$  returns the smallest possible solution, denoted by  $\operatorname{argmin}_{\chi(r)}$  [8]. The previously discussed regularisation method is also used via the term  $\lambda R(\chi)$ , which smooths the output image and reduces artefacts. Due to having to tune the regularisation strength, the image-based methods tended to produce oversmoothed output images. In addition to this, image-based methods involve solving minimisation problems iteratively, converging towards a solution, which is incredibly computationally demanding. All of these different shortcomings resulted in image-based approaches falling short in the QSM challenge.

### 2.2 k-space Methods

An alternative technique that performed exceptionally in the QSM challenge was the use of k-space. K-space-based methods involve using the frequency domain to bypass some of the ill-conditioned aspects of the inverse problem. These methods are incredibly computationally efficient when compared to the image-space-based methods. As a result of this, it is a favourable strategy for large-scale susceptibility mapping studies and clinical applications. It is described by the formula:

$$\chi(k) = \frac{\Delta B_z(k)}{B_0 \cdot d(k)}$$

where  $\chi(k)$ ,  $\Delta B_z(k)$  and  $d(k)$  are the Fourier transforms of  $\chi(r)$ ,  $\Delta B_z(r)$  and  $d(r)$  respectively. This method relies on the convolution theorem, which states that the Fourier transform of a convolution of 2 images is equal to the elementwise product of their Fourier transforms, thereby not having to compute the actual convolution, making the method significantly more computationally efficient. Whilst effective, the accuracy of current k-space methods could be improved. K-space-based algorithms such as thresholded k-space division (TKD) are prone to streaking artefacts in the susceptibility maps, particularly near regions of high susceptibility gradients or boundaries between tissues with susceptibilities of different polarities. Additionally, the ill-conditioned aspect remains, since as  $d(k)$  tends to 0 at  $54.7^\circ$ ,  $\chi(k)$  will tend to infinity. These methods also rely on iterative regularisation, which can again lead to oversmoothing, similar to that found in image-space techniques.[8][12]

### 2.3 The proposed solution

This report proposes a novel solution that draws inspiration from both image-space and k-space methods. By combining key aspects of the two techniques, the new approach aims to overcome their respective limitations, offering a more robust and efficient method for reconstructing susceptibility maps. From the image-space methodology, the proposed solution aims to integrate a physics-based measurement model, and sparsity regularisation optimisation techniques, as per the consensus recommendations, to enhance the fidelity of the reconstructions [13]. This includes addressing challenges such as oversmoothing artefacts, which are commonly encountered due to the iterative optimisation process. The solution also adopts principles from k-space methods by leveraging the convolution theorem as a basis to compute the deconvolution.

Despite the combination of the 2 techniques, there is one common issue that still remains, which is the ill-posed, ill-conditioned nature of the problem, for which the proposed solution will integrate deep learning techniques. Deep learning models have shown

promising results in various medical image reconstruction tasks by learning complex patterns directly from data, bypassing the need for explicit modelling of physical systems. By employing deep learning, the novel method aims to predict deconvolution directly from the input data, eliminating the need for division by problematic denominators. Instead of relying exactly on the convolution theorem and performing the division operation explicitly, the model will be trained to approximate the inverse of the forward problem, which is both well-posed and well-conditioned [14].

A deep learning model will also be able to learn the complex relationship between the input field perturbation and the output susceptibility maps, improving in accuracy through extensive training on a large diverse dataset, following which it will be able to generalise well to unseen datasets and produce high-accuracy reconstructions of susceptibility maps. The proposed solution would have to make use of a memory-efficient deep learning strategy in order to make 3D high resolution reconstructions viable in terms of both computational demand and processing time.

#### 2.4 Monotone Operator Learning & Model-Based Deep Learning

The Dipole Inversion & Susceptibility Map reconstruction programme will be built upon a pre-existing novel framework designed to address inverse problems in imaging, called Monotone Operator Learning (MOL) for model-based deep learning [15]. The MOL approach employs a deep equilibrium algorithm, which aims to find a fixed point solution that satisfies certain specified conditions. This works iteratively, updating the model until it reaches a stable state where the input and output are consistent, effectively solving the implicit inverse problem. The method promises several valuable guarantees. The monotone constraint is stated to be able to ensure uniqueness, rapid convergence, and stability of solutions against input perturbations, meaning that it will not be affected by the ill-posed, ill-conditioned nature of the inverse problem. Traditionally, inverse problems such as image reconstruction have been handled using deep learning via a class of optimisation techniques called unrolled algorithms. The MOL approach aims to surpass these traditional methods by being more memory-efficient, making it ideal for training on large datasets, and potentially applying them clinically. [15]

##### 2.4.1 Monotone Operator Learning Breakdown

An analysis into the effectiveness of MOL as a memory-efficient alternative to unrolled algorithms was conducted. Pramanik et al. (2023) [15] outlines how the MOL framework works, and then compares 2 implementation variations of MOL with the unrolled algorithms. These variations are Spectral Normalisation (MOL-SN) and Lipschitz Regularisation (MOL-LR). [15]

The MOL aims to tackle the inverse problem by approaching it in the form  $b = Ax + n$ , where  $b$  represents the observed data,  $A$  is the measured operator,  $x$  is the unknown image to be reconstructed and  $n$  is the noise via a Gaussian distribution. The objective is to find the maximum a posteriori (MAP) estimate of  $x$  given  $b$ , which is formulated as an optimisation problem. The MAP estimate  $x_{MAP}$  is obtained by minimising a loss function comprising of two terms: a data fidelity term  $\frac{\lambda}{2} \|Ax - b\|_2^2$  and a regularisation term  $\phi(x)$ . Written in full, this is represented by the formula:

$$x_{MAP} = \frac{\lambda}{2} \|Ax - b\|_2^2 + \phi(x)$$

And the minima of this function satisfies,

$$\underbrace{\lambda A^H(Ax - b)}_{\mathcal{F}(x)} + \underbrace{\nabla_x \phi(x)}_{\mathcal{G}(x)} = 0$$

The data fidelity term measures the difference between the observed data  $b$  and the reconstructed signal  $Ax$ , while the regularisation term imposes constraints on the solution  $x$ . The MOL algorithm employs a forward-backward splitting approach that utilises a proximal gradient algorithm to iteratively update the solution  $x$ . While this is not an uncommon method in deep learning architecture, typically separate memory allocations are required for forward and backward passes, leading to higher memory consumption. MOL reduce memory usage substantially by sharing the same single physical layer for both forward and backward propagation, thereby optimising memory usage whilst boasting uncompromised computational efficiency. The forward-backward splitting splits the terms of the minima in the function such that  $\nabla_x \phi(x) = \mathcal{F}(x)$  and  $\lambda A^H(Ax - b) = \mathcal{G}(x)$ , where  $\mathcal{F}$  and  $\mathcal{G}$  represent the gradient of the regularisation term and data fidelity term respectively. At each iteration, the solution is updated using the following rule:

$$x_{n+1} = (I + \alpha \mathcal{G})^{-1}(\mathcal{L} - \alpha \mathcal{F})(x_n)$$

where  $\alpha$  is the step size parameter. This is the simple form of the iterative MOL algorithm, but requires further constraining.

The assumption is made that the operator  $\mathcal{F}$  is said to be  $m$ -monotone if for any pair of vectors  $x$  and  $y$  in the vector space  $\mathbb{C}^M$ , the real part of the dot product of the difference between  $\mathcal{F}(x)$  and  $\mathcal{F}(y)$ , and the difference between  $x$  and  $y$  is greater than or equal to some positive constant  $m$  times the squared L-2 norm of the difference between  $x$  and  $y$ . Mathematically, this condition is expressed as:

This ensures that the difference in output  $\mathcal{F}(x)$  and  $\mathcal{F}(y)$  correspond to the difference in inputs  $x$  and  $y$  such that the operator is monotonically increasing.

There are 2 propositions for Fixed-Point Uniqueness of the monotone operator. The first is that if the operator  $\mathcal{F}$  is  $m$ -monotone (for  $m > 0$ ), the fixed point of the zero gradient equation will be unique to a specific  $b$ .

The second proposition links the Lipschitz constant of the Convolution neural network operator  $H_\theta$  to the monotonicity of operator  $\mathcal{F}$ , providing conditions under which  $\mathcal{F}$  is  $m$ -monotone.[15]

Based on these proposition, the operator  $\mathcal{F}$  is constructed as a residual CNN  $\mathcal{F}$ , with a CNN  $H_\theta$  and Lipschitz embedded in it, expressed as  $\mathcal{F} = \mathcal{L} - H_\theta$ . This CNN contains learnable parameters  $\theta$ , and plays a crucial role in the iterative update process of the MOL algorithm.

Considering all of this information, the iterative MOL algorithm can be reformulated as:

$$x_{n+1} = \underbrace{(I + \alpha\lambda A^H A)^{-1}((1 - \alpha)x_n + \alpha H_\theta(x_n))}_{T_{MOL}(x_n)} + \underbrace{(I + \alpha\lambda A^H A)^{-1}(\alpha\lambda A^H b)}_z$$

Where the update at each iteration involves applying the operator  $T_{MOL}$  and adding a correction term  $z$ . The algorithm iterates until convergence, gradually improving the estimate of the unknown image  $x$ .

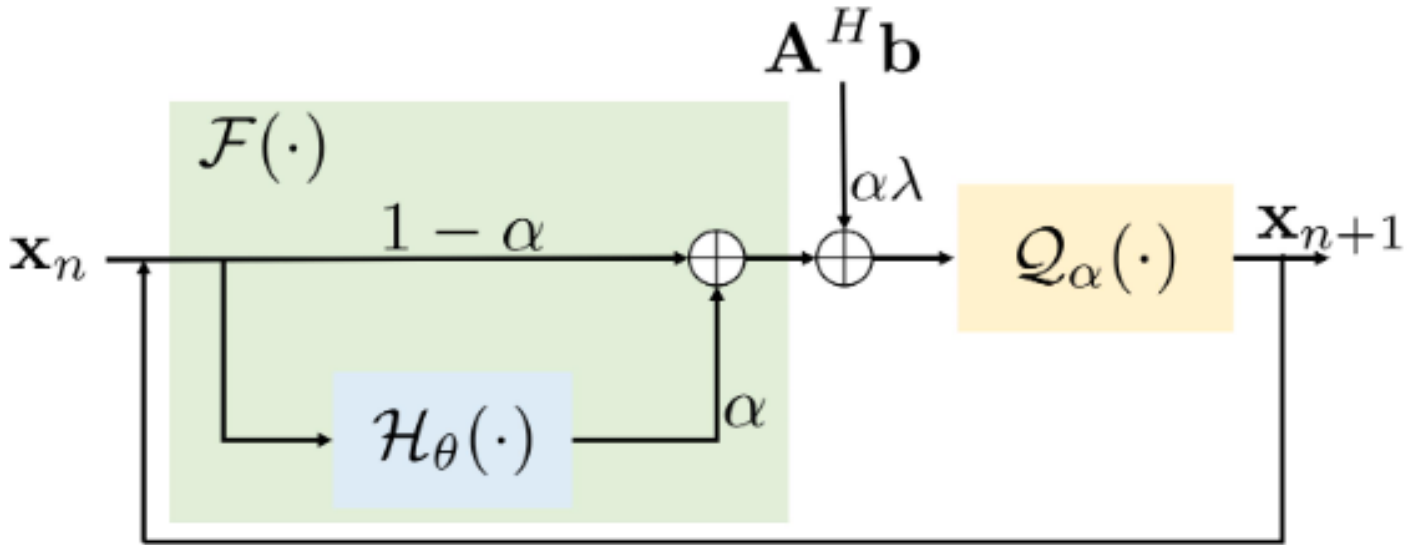


Figure 4 - This is the block diagram representation of the iterative algorithm. [15]

#### 2.4.2 Implementation Variants – Spectral Normalisation and Lipschitz Regularisation

Two variations of stabilisation techniques are implemented in the MOL framework: Spectral Normalisation (MOL-SN) and Lipschitz Regularisation (MOL-LR).

Spectral normalisation is a technique used to stabilise the training of the CNN by estimating the Lipschitz constant of the layer transformations through normalisation of the weight matrices by their spectral norms (maximum eigen value) for each layer in the CNN. A Lipschitz continuous function is one where the absolute difference between the function outputs for any two input points is bounded by a constant multiplied by the spatial distance between the input points. This constant is the Lipschitz constant, and constraining this ensures stability and convergence of the optimisation process, as limiting it will enable the algorithm to prevent large oscillations in the solution, leading to more stable and reliable convergence.[15]



The Lipschitz Regularisation method also aims to stabilise the training of the CNN by estimating the Lipschitz constant, but does this by training a model using a loss function, referred to as the Lipschitz penalty. This Lipschitz constant  $\mathcal{L}[H_\theta]$  is estimated via a maximisation problem:

$$l[H_0] = \max_{x \in S} \sup_{\eta} \underbrace{\frac{\|H_\theta(x - \eta) - H_\theta(x)\|_2^2}{\|\eta\|_2^2}}_{p(x, n)}$$

Where  $l[H_0]$  is the estimated Lipschitz constant,  $\eta$  is the perturbations and  $S$  is the set of training data samples. The perturbations  $\eta$  are solved via  $\eta = \operatorname{argmax}_{\eta} p(x, n)$ , and this estimation problem is solved using a projected gradient algorithm.

### 2.4.3 Supervised Training

Supervised training involves optimising the loss function  $\mathcal{C}(\theta)$  where  $\theta$  represents the parameters of the CNN. This loss function minimises the squared difference between the ground truth  $x_i$  and the fixed-point  $x_i^*$ . There is an additional constraint, which restricts the estimated Lipschitz Constant from exceeding the threshold  $T = 1 - m$ . This constraint is handled via a log barrier method, which converts the constrained optimisation problem into an unconstrained one. The optimisation objective then becomes minimising the sum of squared differences while penalising instances where the Lipschitz Constant exceeds the threshold.

The optimisation problem is described by:

$$\theta^* = \operatorname{argmin}_{\theta} \sum_{i=0}^{N_t} \underbrace{(\|x_i^* - x_i\|_2^2 - \beta \log(T - P(x_i^*)))}_{C_i}$$

### 2.4.4 Performance of MOL-SN and MOL-LR against Unrolled Algorithms

Pramanik et al. (2023) [15] compares the performance of MOL-SN, MOL-LR and Unrolled algorithms to determine whether the MOL framework compromises a substantial enough amount of accuracy in exchange for memory efficiency to the point where it is unviable, and determines which of the two stabilisation techniques is more effective for the MOL framework, SN or LR. The unrolled algorithms that MOL was compared against were SENSE, MoDL, ADMM-Net, DE-GRAD and UNET.[15]

Analysing the results, it is apparent that MOL-SN and DE-GRAD converge more rapidly due to spectral normalization, but exhibit lower overall performance compared to MOL-LR (Fig. 5(b), 5(c)). MOL-LR maintains a Lipschitz constant less than 0.9, indicating stable convergence, and achieves comparable performance to MoDL and ADMM-Net while consuming memory equivalent to a single iteration, significantly less than the unrolled algorithms [16][17]. This makes MOL-LR an attractive option for large-scale problems like 2D+time MRI recovery [18], and puts it in consideration for the proposed Dipole Inversion method.

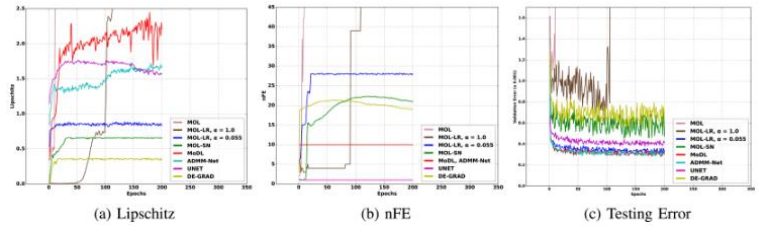


Figure 5 - Training curves for different reconstruction algorithms. [15]

MOL-LR shows robustness to adversarial perturbations, maintaining performance even with 15% Gaussian noise, whereas MoDL, ADMM-Net, and UNET suffer significant performance drops [17]. Despite being Lipschitz-constrained, MOL-LR also maintains competitive performance even without additional noise, making it suitable for practical applications [17].

While MOL-SN converges more rapidly, its overall performance is compromised due to the conservative nature of spectral normalization [17][19]. MOL-LR strikes a balance by maintaining a manageable Lipschitz constant while achieving competitive performance and robustness, making it the preferred option over MOL-SN.

### 2.4.5 Review of MOL Literature

Pramanik et al. (2023) [15] introduces an innovative methodology to tackle image reconstruction, and thoroughly scrutinises this approach against traditional, tried and tested unrolled algorithms. The method is grounded in mathematical principles, particularly around fixed point iterations and Lipschitz, providing a solid theoretical foundation. The evaluation against other algorithms is thorough, and draws conclusions from multiple output metrics, specifically Peak Signal-to-Noise Ratio, and Structural Similarity. The experiments are conducted on real-world datasets, specifically brain, knee and cardiac MRI data, adding to the credibility of the findings and insinuating the potential clinical applications of this technique, which is further emphasised by the core intention of the

research, which was to determine whether this memory efficient method would be a viable alternative to unrolled algorithms; a beneficial property when tackling large-scale real-world problems.

There are some potential criticisms and areas for improvement of the MOL framework and the methodology used to assess it. The methodology would benefit from a comprehensive analysis on hyperparameter sensitivity and devising a method to determine the optimal values for better performance across different datasets and tasks. When applying this method to the Dipole Inversion task, it is unlikely that the hyperparameters currently in place will be optimal, especially since the datasets will be large and three-dimensional. Furthermore, while the method is memory-efficient, it does make use of DEQ solvers and iterative optimisation techniques which increase the computational overhead of the framework, potentially limiting scalability. Applying the MOL model with simpler CNN architectures and assessing the change in performance could prove useful in optimising the balance between computational efficiency and output accuracy.

Ultimately, Pramanik et al. (2023) [15] shows that MOL-LR has the potential to be the ideal method to apply to the Dipole Inversion method. The framework also simultaneously computes the SENSE algorithm, one of the unrolled algorithms, specifically a Conjugate Gradient algorithm, that the MOL was compared to. This will be useful in order to determine whether using MOL will be more efficient than SENSE when trained on the same datasets.

### 3. METHODOLOGY

#### 3.1 Justification of Fundamentals

The primary language chosen for this project is Python. Primarily this is due to the pre-existing framework being written in Python already, making modification simple instead of having to reproduce it from scratch in a different language. There are some benefits that Python has that justify why rewriting it in another language would not be as beneficial. Python is a very versatile language with extensive libraries suitable for deep learning, offering a wide range of ready-to-use tools and packages that facilitate model development and numerical computation. Python is also known for its readability due to its clear syntax and extensive documentation. This makes picking up the unfamiliar framework and adapting it to the needs of this project very easy, thus accelerating the development process. [20][27][28]

Furthermore, PyTorch was chosen as the deep learning framework for this project, as opposed to alternatives like TensorFlow. PyTorch has a wide array of useful existing functions, and enables the creation of custom operators and loss functions with ease, which is crucial for implementing the specialised operations tailored to this image reconstruction task, such as complex-valued convolutions, k-space data manipulation and Lipschitz regularisation. PyTorch also provides seamless GPU acceleration, allowing for efficient utilisation of GPU resources to speed up training and inference, which will drastically reduce training times and enable the handling of high-resolution, large MRI images and real-time reconstruction scenarios that are crucial for clinical applications.

#### 3.2 The Forward and Adjoint Operators

The Forward ( $A$ ) operator is the operation that is performed on  $x$  to produce  $b$  in the  $b = Ax + n$  model. In other words, the forward operator  $A$  is the function that's having it's inverse approximated via the MOL and Model-based Deep Learning framework. For the context of the dipole inversion, the forward problem is simply the convolution between the input image  $x$  and the dipole kernel  $k$ . Utilising the convolution theorem, this operation can be performed more efficiently by formulating the elementwise product of the dipole kernel and the image in k-space. The elementwise product between  $X$  and  $K$  is equivalent to taking the matrix multiplication between  $X$  and a diagonal matrix  $D$ , where the values along the diagonal of  $D$  are all of the elements of  $K$  in row-major order. [21]

Fourier transforms can be computed in various methods, with one of the most efficient being the Fast Fourier Transform (FFT). FFT is an algorithm that calculates the Discrete Fourier Transform of a sequence. The Discrete Fourier Transform (DFT) can be expressed as a transformation matrix called a DFT matrix. The FFT process can be expressed mathematically as the multiplication:

$$X = Fx$$

where  $x$  is the input matrix in image space,  $F$  is the N-by-N square DFT matrix and  $X$  is the DFT of the input matrix, i.e. the input image in k-space. The FFT process can be leveraged to perform the convolution as a series of matrix multiplications, which can be written as:

$$Ax = (F^H DF)x$$

Where  $F$  is the DFT matrix, which when multiplied with input image  $x$ , takes the Fourier transform and outputs  $X$ , the input image in k-space.  $K$  is the dipole kernel in k-space, which is multiplied elementwise with  $X$ . The elementwise product of  $K$  and  $X$  is then multiplied by the conjugate transpose  $F^H$  of the DFT matrix, which performs the inverse Fourier transform, returning the output image to image-space. The result of this is the convolution between the input image  $x$  and the dipole kernel  $k$  in a computationally efficient manner.

The MOL algorithm also requires the adjoint operator  $A^H$  must also be provided. The adjoint operator is the conjugate transpose of the forward operator. Given the structure of the forward operator, performing the conjugate transpose  $A$  is relatively straightforward.

$$A = F^H DF$$

$$\therefore A^H = (F^H DF)^H$$

There are 2 key properties of conjugate transpose that can be leveraged to simplify this operation. [22]

- 1)  $(QR)^H = R^H Q^H$  for any  $m \times n$  matrix  $Q$  and any  $n \times p$  matrix  $R$ . Note that when expanded, the order of the matrices is reversed.
- 2)  $(Q^H)^H = Q$  for any  $m \times n$  matrix  $Q$ , ie The conjugate transpose is a self-inverse function.

Using these properties,  $A^H$  can be simplified as follows:

$$A^H = (F^H D F)^H$$

$$A^H = F^H D^H (F^H)^H$$

Since  $D$  is a diagonal matrix where the values along the diagonal of  $D$  are the elements of  $K$  in row-major order,  $D$  is a symmetrical matrix, thereby meaning  $D$  is a Hermitian matrix, ie a matrix that is equal to its own conjugate transpose. With this identity, the simplification of  $A^H$  can be progressed as follows:

$$A^H = F^H D^H (F^H)^H$$

$$A^H = F^H D F = A$$

This simplification shows that conjugate transpose of the operator  $A$  is itself, indicating that the forward operator and the adjoint operator are the same.

To summarise, the forward  $A$  and adjoint  $A^H$  operators for performing convolution between an input image  $x$  and a dipole kernel  $k$  are defined as:

$$A = A^H = F^H K F$$

Where  $F$  is the DFT matrix,  $K$  is the dipole kernel in k-space, and  $F^H$  is the inverse DFT matrix.

### 3.3 2D Convolution and Deconvolution

Prior to implanting the 3<sup>rd</sup> dimension, the functionality of the operators had to be validated in 2 dimensions. To first assess whether the convolution works correctly, a set of simple test images were created. For the input image, a  $50 \times 50$  voxel torus 2D image was generated, and for the kernel, a 50 by 50 magic square. For simplicity and ease of analysis, the torus was comprised entirely of ones and the surrounding area was entirely zeros. Having non-random input images and kernels was important to enable comparisons between attempts to assist debugging.

As shown in *Fig 7*, the convolution operator, and the conjugate gradient inverse algorithm both function as intended. The inverse of the data model applied to the convolved image  $b$  produces an image that is virtually identical to  $x$ . The forward operator also functioned as expected, producing a convolution between  $x$  and the magic square kernel, evident by the streaking and ‘ripple-like’ artefacts on the torus.

The success of this indicates that the operators function correctly when directly computing the inverse via Conjugate Gradient (CG) optimisation. The MOL algorithm was then run parallel to the CG SENSE algorithm, both over the course of 20 epochs, to produce outputs with identical parameters for comparison of the efficacy of the methods.

### 3.4 2D to 3D Framework Modification

Modifying the framework to be able to handle 3D data requires parsing the code and identifying all functions and methods used that pertain to the dimension of the input image. This primarily involved altering the FFT functions such that they addressed 3 dimensions by using 3D DFT matrices instead of 2D, correcting the forward and inverse Fourier shift functions to ensure that the images were shifted in 3 dimensions and then re-centred around zero correctly, etc. The core algorithm did not require any changes since susceptibility is a dimensionless measurement. Provided that the dimensions are consistent throughout the algorithm and the dimension-specific functions are appropriately set for the dimensions of the input data, it will perform correctly and output an image with the same number of dimensions as the input images.

Once the code was suitable to address the additional new dimension, new test images were also generated. For the input image  $x$ , a simple  $50 \times 50 \times 50$  image of a sphere was used, where the sphere was comprised entirely of ones and the surrounding area was entirely zeros. A simple kernel was also generated. The kernel was a  $50 \times 50 \times 50$  image consisting of a checkerboard pattern of ones and zeros, with each square of this 3D checkerboard being  $5 \times 5 \times 5$ . Using a kernel that is easily distinguishable through just visualisation, without the use of analytical functions and metrics, is useful during testing as, similar to the 2D convolution tests, identifying errors, especially pertaining to dimensionality in this case, would be much faster. Using metrics is effective in more intricate cases, such as assessing structural similarity or noise, but these metrics only provide comparative data, and don’t provide recommendations on how to resolve the issue, or which functions could have been incorrectly modified to 3D. Being able to notice

patterns in the output images that aren't expected, simply by observation, will not only aid with identifying an issue is present, but also with diagnosing the issue.

As shown in *Fig 7*, the model is able to handle the 3<sup>rd</sup> dimension as expected, convolving the sphere with the 3D checkerboard kernel correctly. At this point, the 2D MOL framework has successfully been modified into 3 dimensions, meaning it is ready to be adapted and used to handle 3 dimensional image reconstruction problems, simply requiring the forward and adjoint operators to be altered to fit the new problem.

### 3.5 Visualising and Implementing the Dipole

The algorithm is capable of handling the convolution operation and approximate it's inverse in three dimensions. In other words, the programme currently performs three-dimensional kernel inversion on an input image. The only modification left to do before the programme can perform dipole inversion is to actually implement the dipole. As per QSM consensus, the dipole kernel is defined as:

$$d(r) = \frac{3 \cos^2 \theta - 1}{4\pi r^4}$$

The convolution of the kernel with an input image using the convolution theorem requires both the image and the kernel it is being convolved with to be in the frequency domain. For this to be the case, the Fourier transform of  $d(r)$  must also be found. This can be done via the FFT method used for the input image  $x$ , however a more computationally efficient method would be to simply generate the 3D dipole in k-space, ie generate  $d(k)$  instead of  $d(r)$ . In the Fourier domain, the dipole kernel can be defined as follows: [26]

$$d(k) = \frac{1}{3} - \frac{k_p^2}{|k|^2}$$

$$k_p = \vec{k} \cdot \vec{B}_0,$$

Where  $k_p$  is the component of the wave vector perpendicular to the magnetic field direction,  $B_0$  is the direction of the magnetic field vector,  $|k|^2$  is the magnitude of the wave vector and  $\vec{k} = (k_x, k_y, k_z)$ .

This is implemented in code via a dipole creation function, which works by first generating meshgrids for  $k_x, k_y$  and  $k_z$ , spanning the same data shape and size as the input image  $x$ . Then, the function normalises these vectors based on voxel size and maximum absolute values. It then computes  $k^2 = k_x^2 + k_y^2 + k_z^2$ , replacing any zeros with a very small value to avoid 'division by zero' errors. These values are then input into the formula for  $d(k)$ , returning a k-space dipole kernel with a size and shape identical to the input image  $x$ .

The algorithm with the updated k-space dipole kernel was applied to the simple sphere input image in order to validate the dipole and the dipole inversion.

### 3.6 3D Dipole Inversion

200 sophisticated  $64 \times 64 \times 64$  voxel images, comprised of different 3D overlapping shapes of varying intensities, were generated. Using SENSE, the unrolled algorithm that is being compared to MOL, the forward operator is applied to these input images  $x$ , convolving each of them with the dipole kernel to produce a training dataset of 200 simulated 3D phase images. By developing the training data using this method, the original 200 unconvolved images will be the ground truth. The MOL algorithm will be able to compare the image reconstructions produced using the simulated phase data to the ground truth data and improve its reconstruction. A large dataset size is used to train the model on a wide range of data, which prevents overfitting and improves robustness.

Note that since the forward operator is applied to the input images to produce the simulated phase images, the SENSE reconstruction of the dipole inversion will be of a higher accuracy, since it is essentially inverting it's own forward operation. The MOL's performance will still be compared to the SENSE's performance, however it is crucial to understand that conclusive decisions regarding MOL's effectiveness should be made with this information in mind.

### 3.7 Hyperparameter Tuning

There hyperparameters considered for tuning were the number of Epochs, the Learning Rate of the Model, the initial Lambda Value, the Lambda Iterations, the Filter Size and the Number of Layers.

Based on prior testing, the output accuracy seemed minimally influenced by factors influencing Lambda, ie the initial value and the number of iterations, since the model eventually corrected for them regardless. Learning rate did have a slight influence on the rate of

convergence to a solution, but again this had minimal impact, as it would only result in the number of epochs to reach an error plateau to be slightly longer. The hyperparameters that had the greatest influence on the accuracy and efficiency of the output were the Filter Size and the Number of Layers.

The term Filter size refers to the dimensions of the filter or kernel, in this case the dipole kernel, that is convolved with the input data. Smaller filter sizes allow the model to capture finer details and local patterns in the input data, whereas larger filter sizes capture more global features. Since for this context the aim is to visualise magnetic dipole interactions throughout the image, having a larger filter will allow the interactions to be more similar to how they are in real life. Increasing the filter size can increase the receptive field of each neuron in the convolution layers, enabling them to capture more complex patterns. However, larger filters also increase the number of parameters in the model, which can result in overfitting, especially if the dataset is small. The larger filters also require more computation as they compute more operations per convolution, meaning that each epoch of training will take longer to compute. Striking a balance between capturing more complex patterns whilst avoiding overfitting and excessive computational demand is crucial when trying to make this model as efficient as possible, potentially even for clinical applications.

The number of Layers in general deep learning model refers to the total count of layers, which can include convolutional layers, pooling layers, fully connected layers etc. In the MOL, the 'Number of Layers' parameter pertains to the number of convolutional layers within a depth-wise convolutional block, which iteratively creates the convolutional layers and sequentially applies them to the input data. Therefore, adjusting the number of layers controls the depth and complexity of the convolutional block. More layers have the capacity to learn hierarchical representations of the input data, with each layer learning increasingly abstract features, allowing the model to capture more complex relationships in the images. This enhances the model's expressiveness, meaning it can learn more intricate patterns and relationships in the data, resulting in better performance on complex tasks. Once again however, a balance must be struck since deeper networks are more prone to overfitting. A higher number of layers will increase the model's capacity to memorise the training data, resulting in poor performance when the model is applied to unseen data. Like the Filter Size, increasing the number of layers also increases the computational cost, memory requirements and training time.

Both Filter Size and the number of layers influence the number of weights that the model has. In deep learning, weights refer to the parameters that the neural network learns during the training process. These weights can be described as numerical values that the network adjusts iteratively to minimise the difference between the predicted output and the actual target output for a given input. These weights are adjusted based on this error via a process known as backpropagation, which leverage optimisation algorithms, in this case the Adam optimisation algorithm. The number of weights in the model can be determined by:

$$w = f \times l$$

where  $w$  is the number of weights,  $f$  is the size of the filter (e.g. a filter size of 5 would be a  $5 \times 5 \times 5$  filter, giving it a size  $f = 125$ ), and  $l$  is the number of layers.

The optimal Filter Size and Number of Layer combination was determined by comparing the accuracy of the output images for all reasonable combinations. The metric for accuracy used throughout the methodology is Structural Similarity and Peak Signal to Noise Ratio, metrics commonly used to evaluate the quality of reconstructed images. Structural Similarity (SSIM) returns the similarity between the predicted output and the actual target output as a percentage. Peak Signal to Noise Ratio (PSNR), expressed in decibels (dB), provides a quantitative measure between the intensity of the most intense voxel in the output image, and the intensity of the corrupting noise that affects the fidelity of the output image. The formula for calculating PSNR is:

$$PSNR = 10 \cdot \log_{10} \left( \frac{MAX^2}{MSE} \right)$$

where  $MAX$  represents the maximum possible voxel value of the image, and  $MSE$  is the Mean Squared Error between the original and reconstructed images, calculated as the average of the squared difference between the corresponding pixels in the two images. Higher PSNR values indicate better quality reconstruction as they suggest lower distortion between the original and reconstructed images. Using both of these metrics provides a comprehensive assessment of the accuracy of the outputs.

As shown in Fig. 6, the most efficient combination was a filter size of 35, and 7 layers, as they provided the highest metric values, with an SSIM of 99.56% and a PSNR of 44.22dB, indicating the most accurate reconstruction. Having such a deep neural network will result in epochs taking longer, however this issue can be mitigated by leveraging the power of High-Performance Computing (HPC) [24][25].

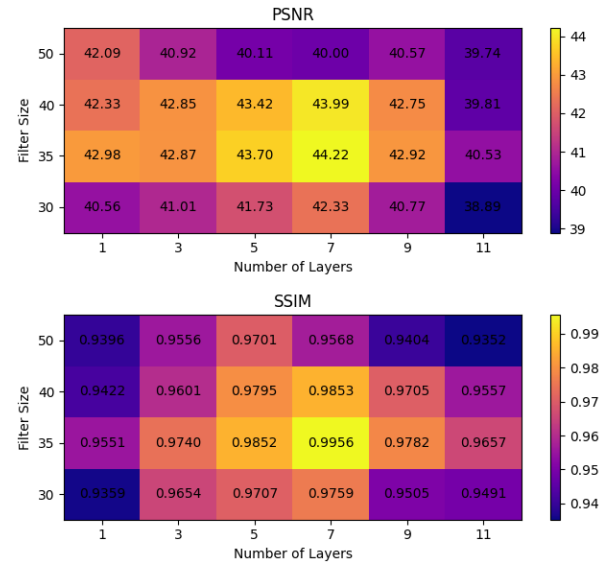


Figure 6 - PSNR and SSIM grid, for combinations of varying numbers of layers and filter sizes

### *3.8 Multiple Batch Model Training*

The accuracy of the model's reconstruction of the susceptibility map are improved when trained on more data, as this optimises the weights such that they ensure the least error between the reconstructed susceptibility map and the actual susceptibility map as possible. The model was trained on 100 different  $50 \times 50 \times 50$  simulated phase images, for a total of 30 epochs, with a Filter size of 35, and 7 layers. To improve the time-efficiency of the training method, the input images were organised into batches. This allows the processing of multiple data samples together in a single forward and backward pass through the neural network.

To handle this amount of data, and allow them to be processed on the same layer, powerful hardware is required. GPUs excel at parallel computation, and are typically used for deep learning training. Large batch sizes also demand more RAM in order to store the necessary data structures during training.

High-Performance Computing (HPC) is the use of computer clusters, with significant processing power and memory, to handle computationally demanding tasks. [24] For this project, a cluster was selected that uses the NVIDIA 40G A100s GPU, and utilises 16GB of RAM. This proved sufficient for batch sizes of 15, for images of size  $50 \times 50 \times 50$  voxels. Note that RAM demand increases linearly with batch size. Batch sizes don't influence the accuracy of the resolution, and only serve to leverage the high RAM availability to reduce the training time.

### *3.9 3D Large Brain Image Susceptibility Map Reconstruction*

The Dipole Inversion algorithm is completed and optimised, meaning that it can be applied to an MRI brain phase scan in order to reconstruct an actual brain quantitative susceptibility map. The input brain phase image used for this reconstruction is larger than the test data, with a size of  $164 \times 205 \times 205$  voxels. While this can be input as it is, it would require the dipole kernel to also be  $164 \times 205 \times 205$ . Changing the image size would require retraining the model on entirely  $164 \times 205 \times 205$  simulated phase images. A different, large image size would also mean the filter sizes would have to be retuned and the number of weights would be very large, increasing the computational demand.

An alternative method to handling this larger image size more efficiently is splitting the image into patches. The patches will have the same size as the images the model was trained on, those being  $64 \times 64 \times 64$ . The stride used for the patching process will be 32, meaning that there will be overlap in every patch. This will result in a total of  $4 \times 5 \times 5$  patches, i.e. a total of 100 images for the model to reconstruct. Finally during the stitching process, overlapping voxels are averaged to produce the final value of the voxel. Since the number of images being reconstructed is 100, there will be a high computational demand. To handle this, the same HPC cluster used for training will be used again[24]. The predicted output for both the SENSE and the MOL algorithms will be assessed by determining each of their accuracy via the SSIM and PSNR metrics and comparing them.

In initial testing there were some issues as a result of the stitching, resulting in significant noise and artefacts along the stitch lines, however by adjusting the stride length to being half of the patch sizes, it distributes the noise caused by the stitching and averaging across the entire image, ultimately reducing the PSNR. Whilst this is not ideal, the only way to truly resolve and prevent any stitching-related noise would be to not use patching at all, and let the model be trained and tested on  $164 \times 205 \times 205$  images, however the computational power at the project's disposal is not sufficient for this to be a viable option.

### *3.10 Methodology Summary*

To summarise, the methodology outlines the logical processes behind the modifications made to the MOL framework detailed in Pramanik et al. (2023) [15] to focus on dipole inversion for QSM. The forward and adjoint operators for convolution were defined, and the framework was successfully adapted to handle 3D data. Hyperparameter running was conducted to optimise the model's performance, with filter size and number of layers identified as the critical factors. Training was performed on batches of simulated data using high-performance computing resources to decrease runtime. The reconstructions of the large brain susceptibility maps were efficiently handled by splitting the image into patches and stitching the results.



## 4. RESULTS AND ANALYSIS

### 4.1 2D SENSE vs MOL

The results of the 2D simple torus test show that firstly both the MOL and SENSE have both successfully inverted the kernel convolution. The reconstructed output images are visually almost identical to the ground truth image.

The training parameters were: 50 training epochs, a learning rate of 0.001, a filter size of 64 and 1 layer.

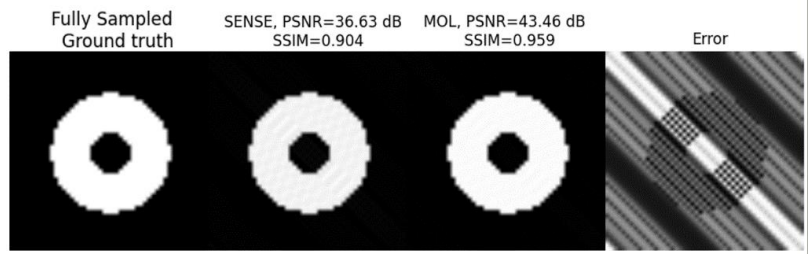


Figure 7 - 2D binary torus reconstruction, SENSE vs MOL

The results of the 2D validation test show that the MOL outperformed the SENSE algorithm, achieving a 5.5% greater structural similarity, indicating a more accurate reconstruction to the ground truth.

The MOL output also had a better Peak Signal to Noise ratio of 43.46dB, compared to the SENSE output's PSNR of 36.63dB. There is some slight error when comparing the ground to the MOL output, as is visualised by the 4<sup>th</sup> image by magnifying the colour scale so that the error is visible. In the reconstruction images, the error is unnoticeable visually, meaning the error can be considered insignificant. This type of error is a non-issue due to two reasons. The MOL and SENSE outputs are approximations of the Ground truth. Because of this, there will always be some slight difference between the reconstructions and the ground truth. Secondly, since ultimately the observers of the QSM reconstruction images will be human diagnosticians, clinicians, etc., errors that are not visible to the naked eye are inconsequential. Overall, these results constitute a successful 2D reconstruction.

### 4.2 3D SENSE vs MOL: Simple Sphere

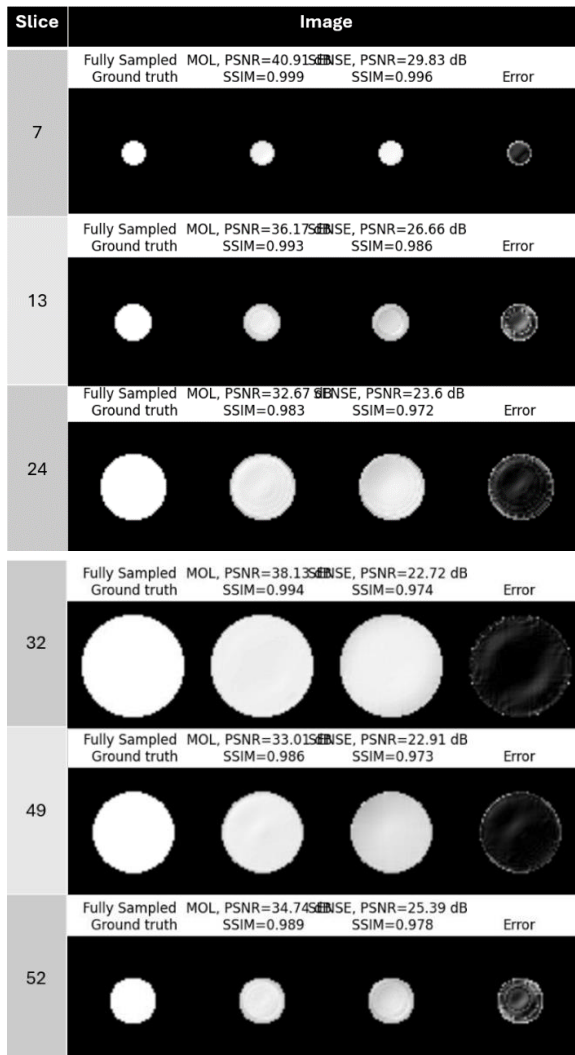


Figure 8 - Slices extracted from 3D reconstructions of binary sphere, MOL vs SENSE

The results of the 3D simple sphere test show that firstly both the MOL and SENSE have both successfully inverted the kernel convolution. The reconstructed output images are visually almost identical to the ground truth image.

The training parameters were: 40 training epochs, a learning rate of 0.001, a filter size of 64 and 3 layers.

[FIG] shows slices 18, 32 and 54 of the 3D ground truth image, the MOL reconstruction and the SENSE reconstruction, as well as the error, which visualises the difference between the MOL output and the ground truth, by amplifying the magnitude of the difference so that it is visible.

The MOL outperformed the SENSE model in every single slice of the three-dimensional image. The SENSE image performed consistently throughout all slices, achieving an average of 98.34% structural similarity across all slices. The MOL performed at or above this level at every slice. For the middle slice (32), as well as slices such as 13 and 7, the MOL performs virtually perfectly, achieving a structural similarity of 99.4%, 99.9% and 99.3% respectively, where the SENSE algorithm was only able to achieve 97.4%, 99.6% and 98.6% respectively. The MOL reconstructions also had less noise, as is shown by the PSNR being greater for the MOL than the SENSE outputs in every slice. Overall, these results support the statement that the MOL can successfully approximate deconvolution of simple binary images to a high degree of accuracy.



#### 4.3 3D SENSE vs MOL: Simulated Phase (Training, Non-comparative)

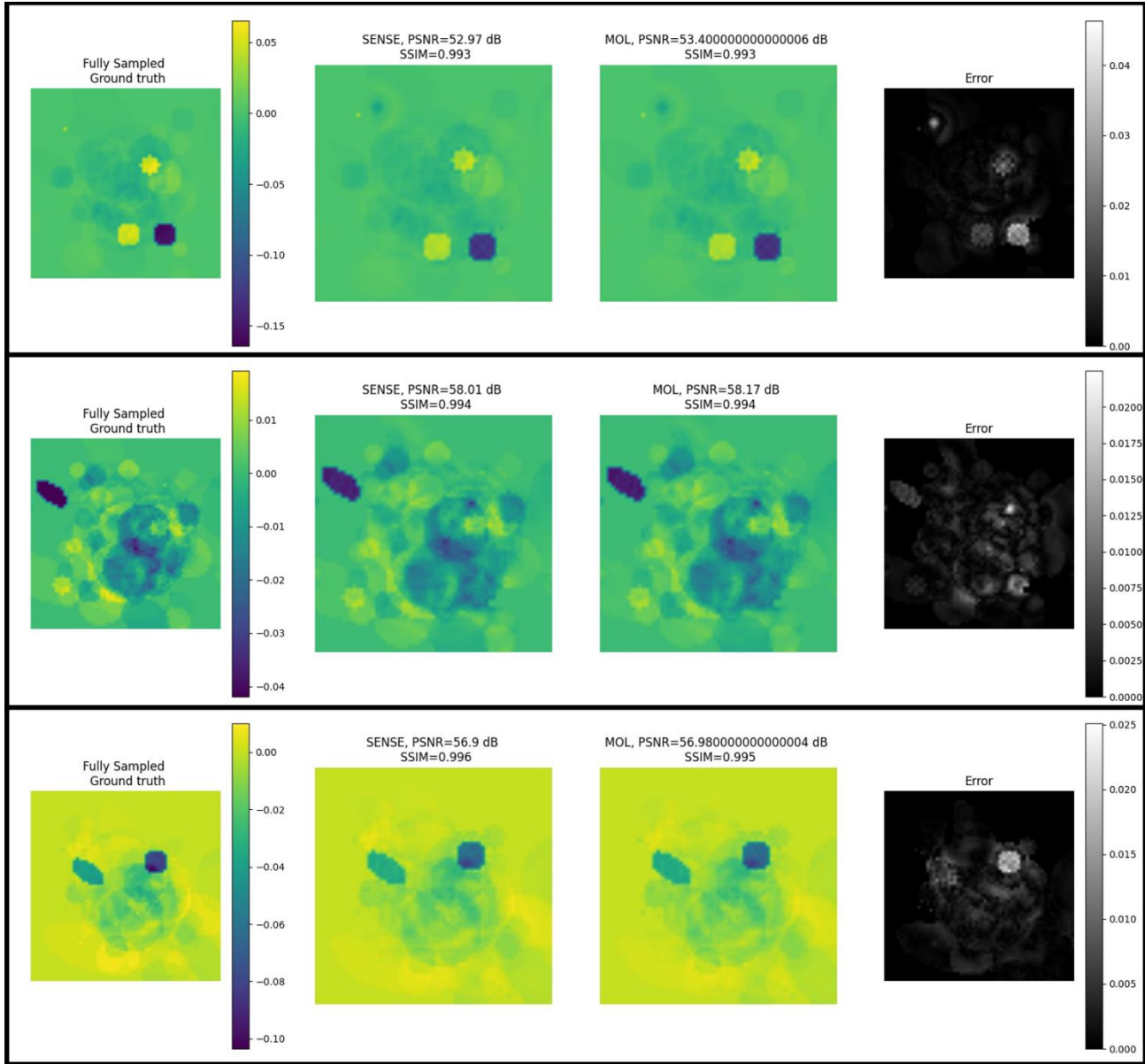


Figure 9 - 3D dipole inversions of simulated input images, SENSE vs MOL

(Slices taken from different datasets to illustrate consistency of performance)

This is the dipole inversion performed on simulated input data. As previously stated in section 3.6, for this training and testing, the input data for both MOL and SENSE are simulated images that were constructed by applying the forward operator to the ground truth data.

The training parameters were: 30 training epochs, a learning rate of 0.001, a filter size of 35 and 7 layers. After training on 100 datasets, these are the results of the algorithms applied to 3 unseen validation 3D input images. For the reconstruction, since SENSE is essentially inverting it's own operation, SENSE has performed significantly better than expected, achieving a structural similarity of greater than 99% on all slices of the 3D images. MOL has also been able to achieve a structural similarity of greater than 99% on all slices, always either equalling or within 0.2% below the structural similarity achieved by SENSE for any slice.

Surprisingly, MOL has outperformed SENSE in every slice for the PSNR metric, achieving around 0.1dB greater than SENSE. Nevertheless, both algorithms performed very well in terms of both SSIM and PSNR, therefore these results support the statement that the MOL can successfully approximate deconvolution of more sophisticated non-binary images to a high degree of accuracy.

#### 4.4 3D SENSE vs MOL: Brain Image QSM Reconstruction

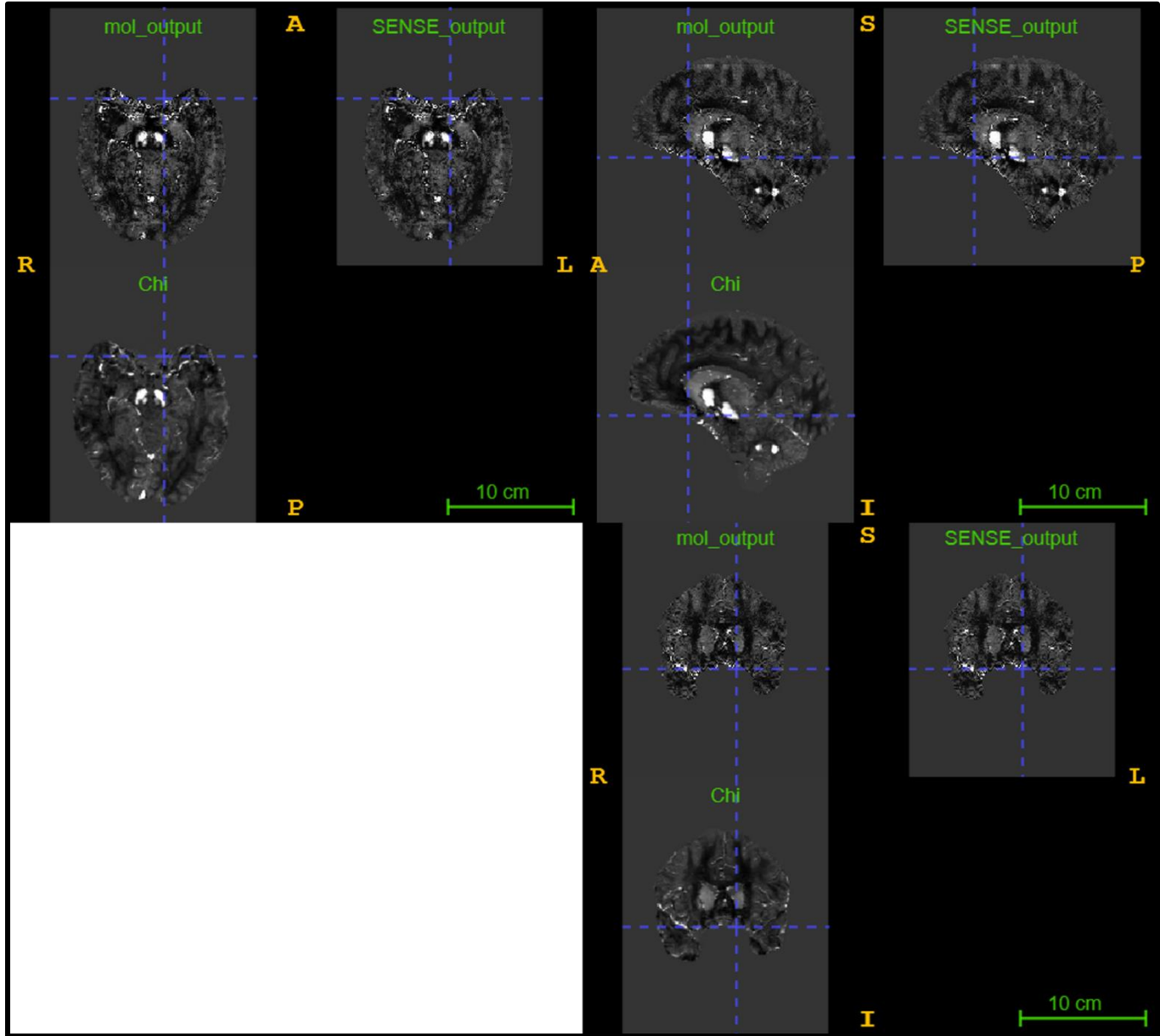


Figure 10 Slice A - 3D brain dipole inversion susceptibility map reconstruction. Axial [upper left], Sagittal [upper right], Coronal [bottom right]. Each view contains MOL and SENSE reconstructions, as well as ground truth image

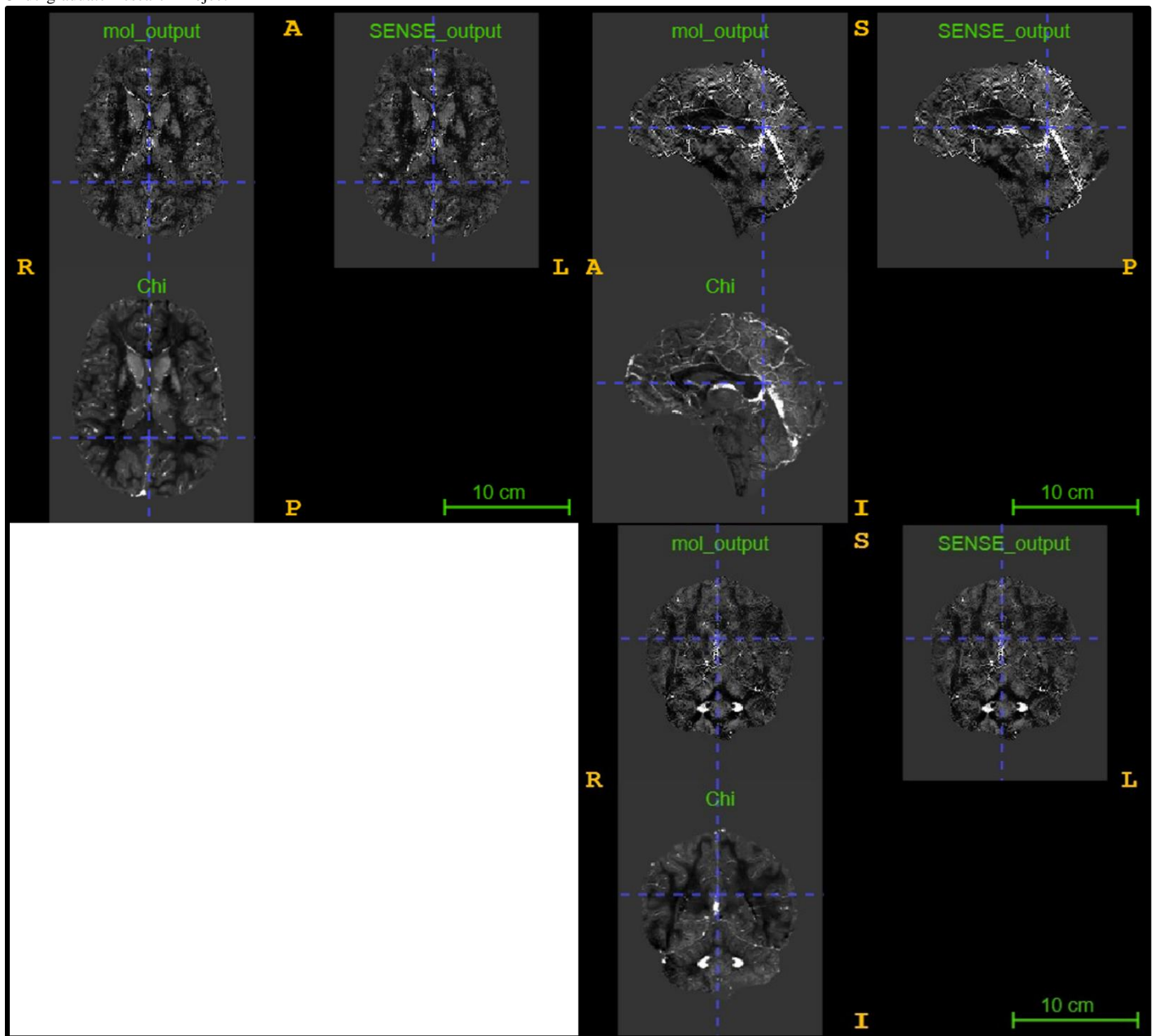


Figure 10 Slice B - 3D brain dipole inversion susceptibility map reconstruction. Axial [upper left], Sagittal [upper right], Coronal [bottom right]. Each view contains MOL and SENSE reconstructions, as well as ground truth image

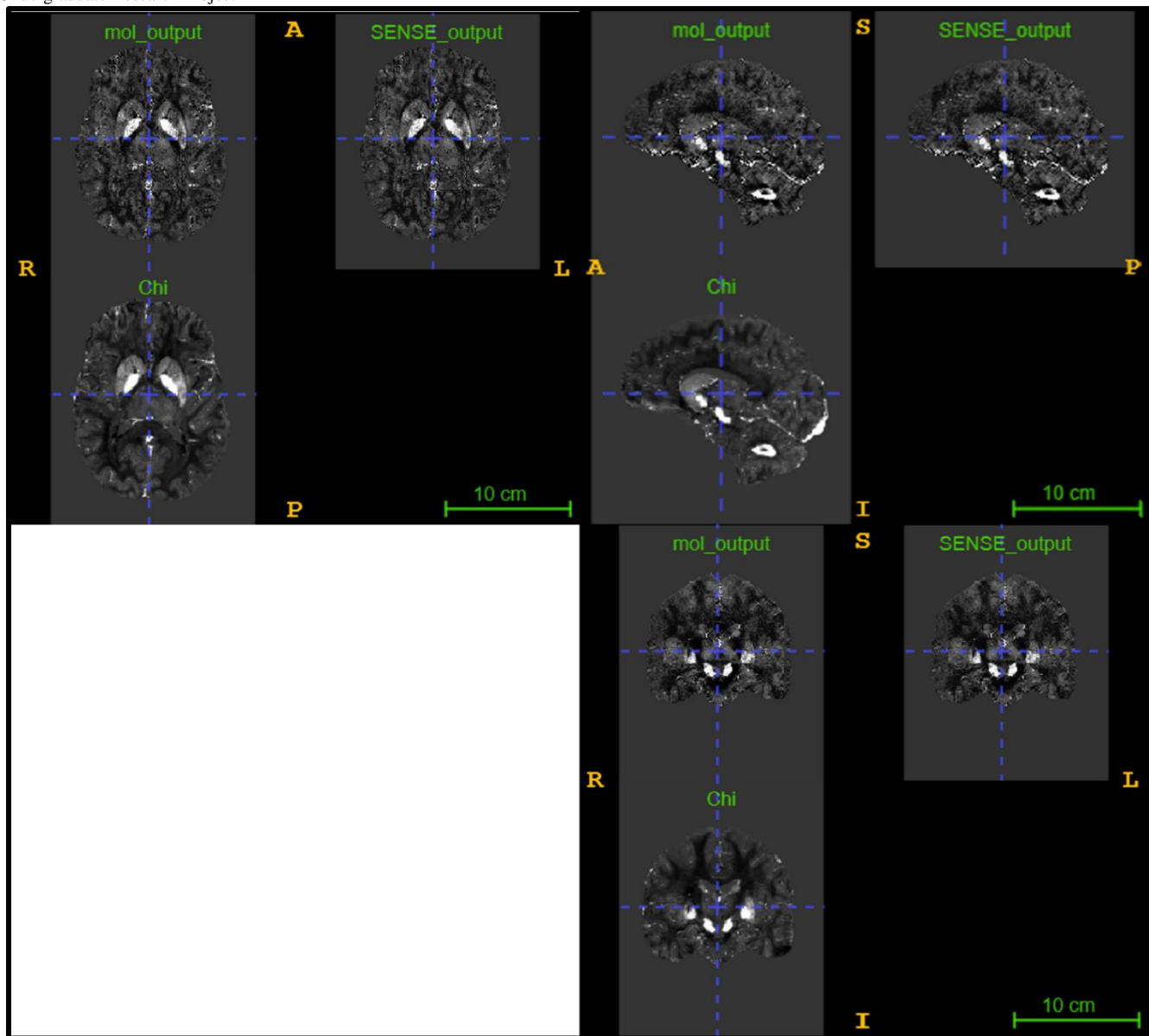


Figure 10 Slice C - 3D brain dipole inversion susceptibility map reconstruction. Axial [upper left], Sagittal [upper right], Coronal [bottom right]. Each view contains MOL and SENSE reconstructions, as well as ground truth image

SSIM		PSNR	
MOL	SENSE	MOL	SENSE
80.6%	72.4%	12.54	7.13

Figure 11- SSIM and PSNR for 3D brain image, MOL vs SENSE

The results of the 3D Brain Image QSM reconstruction show that the MOL was able to reconstruct a susceptibility map of the brain successfully, achieving a visually similar output to the SENSE algorithm.

The model had preloaded the weights obtained through training on the simulated phase dataset. The training parameters were: 30 training epochs, a learning rate of 0.001, a filter size of 35 and 7 layers. After training on 100 simulated phase images, these are the results of the algorithms applied to the unseen brain image after 30 epochs.

Due to the high resolution and intricate, robust nature of the images, it was anticipated that the outputs of both SENSE and MOL wouldn't be as accurate as for the previous tests on less complicated images. There is some visually identifiable noise on both the MOL and SENSE outputs, which can be attributed to the stitching and patching process outlined in section 3.9.

As shown by Fig 10, the MOL outperformed SENSE once again in both metrics, achieving a significantly greater SSIM and PSNR. These results support the statement that the MOL can successfully approximate deconvolution large high-resolution brain images to a higher degree of accuracy than the CG-SENSE algorithm.

## 5. DISCUSSION

In this paper, an alternative method to traditional dipole inversion methods for QSM was presented and tested, that utilised model-based deep learning and monotone operator learning, promising to be more memory efficient without sacrificing on accuracy and precision. Compared with the traditional CG-SENSE unrolled algorithm, the novel MOL algorithm demonstrated superior memory efficiency whilst not only maintaining a similar accuracy to the CG-SENSE model but surpassing it.

All 3 comparison experiments between the MOL and SENSE (CG unrolled) algorithms show that the MOL is able to perform the dipole inversion and reconstruct three-dimensional susceptibility maps with a higher accuracy than SENSE, a traditional unrolled algorithm that utilises the Conjugate Gradient method [23]. In the 2D torus binary image test, and for every slice of the 3D sphere binary image test, MOL outperformed SENSE in both the Structural Similarity metric and the Peak Signal to Noise Ratio metric. As for the more complex, higher resolution brain image, the MOL again significantly outperformed SENSE in Structural Similarity and PSNR. The MOL model was able to outperform the SENSE model due to the extensive training and optimisation it underwent, resulting in it being able to approximate the deconvolution operation with great effectiveness. Moreover, in all tests, the MOL remains memory and computationally efficient by performing the forward and backward passes of the algorithm on the same layer, leading to low RAM usage and short processing times. Key characteristics of algorithms used in this context are their ability to produce accurate results, be memory and time efficient, and be computationally efficient. In all these facets, the MOL model has exceeded the SENSE model, demonstrating a superior alternative to traditional dipole inversion.

While the MOL algorithm presents a powerful advancement in MRI QSM reconstruction, there are several avenues for further research and improvement. Immediate improvements that can be made to the current methodology is training the model on brain phase and brain susceptibility map images, as opposed to the arbitrary simulated images used in this paper. Doing so would allow the model to discern intricate patterns in the brain, be able to minimise noise in the output and produce more accurate brain susceptibility images. Using real brain images wasn't viable for this project due to time and other logistical constraints. Ensuring patient data privacy and confidentiality is paramount, and safeguarding sensitive medical information via data anonymisation and encryption protocols would be a lengthy process, which would reduce the time allocated for developing and optimising the model.

Furthermore, the brain input image has a size of  $164 \times 205 \times 205$  voxels. Due to hardware limitations and time constraints, training the model on a large dataset containing  $164 \times 205 \times 205$  input images, or simply running the final test on the  $164 \times 205 \times 205$  brain image, would require an incredible amount of memory. To handle this, a patching and stitching method was used, however this introduces noise due to the nature of this process. While the noise is minimal, and the MOL output is still more successful than the SENSE output, the MOL output could easily be further improved by allocating more powerful resources in order to train the model on  $164 \times 205 \times 205$  images and process the brain image without the need for patching and stitching. Producing outputs with less noise is crucial for the interpretability of the susceptibility maps, which is arguably the most important aspect of the output due to the clinical relevance and utility of the images. Radiologist and clinicians must be able to easily interpret the results for diagnostic and/or research purposes, and having noise, streaking and other artefacts impairs their ability to do so, particularly for tasks such as segmentation, tumour and lesion detection and classification, and vascular imaging. Mitigating these issues will strengthen the algorithms appeal for adoption in medical imaging practices.

For future research and expansion on this MOL algorithm, exploring different loss functions and regularisation techniques could also enhance the robustness and generalisability of the outputs. Investigating the scalability of the MOL framework, and potentially the success and compatibility with even simpler CNN architectures could facilitate broader adoption and deployment in clinical settings, ensuring widespread accessibility to the benefits of QSM. Aside from the technical improvement of the model, validation studies conducted in clinical settings will also be crucial for demonstrating the real-world efficacy and reliability of the MOL algorithm for healthcare professionals.

## 6. CONCLUSION

Quantitative Susceptibility Mapping in MRI imaging is a novel method of processing MRI data to reveal valuable insights into the microstructure of tissue, notably brain tissue. This paper presented an innovative approach utilising model-based deep learning and monotone operator learning to handle the ill-posed dipole inversion problem - the final stage of the QSM pipeline - for 3D data. MOL possesses key advantages including memory efficiency and lower computational intensity. Extensive testing was conducted to compare the MOL approach to a traditional SENSE algorithm, including 2D and 3D images, & a 3D brain image, ultimately demonstrating superior accuracy and efficiency, and thereby potential clinical viability of MOL. The MOL algorithm has significant implications for clinical practice, enabling improved imaging and diagnosis in fields like neurodegenerative disease detection. Further advancements and optimisations of the MOL algorithm using more powerful hardware could lead to widespread adoption in medical imaging facilities, improving patient outcomes.



## ACKNOWLEDGMENT

I would like to express my sincere gratitude to my primary supervisor, Patrick Fuchs, for his invaluable guidance, unwavering support, and insightful feedback throughout the course of this research project. His expertise and support have been instrumental in shaping my understanding and success in this project. I would also like to extend my thanks to my secondary supervisor, Jannete Nassar, for her valuable input, constructive criticism, and dedication to ensuring the success of this endeavour. Her input and encouragement have greatly enriched this research journey. I am deeply appreciative of the support and encouragement provided by both supervisors, without which this research would not have been possible.

## REFERENCES

1. Magnetic Resonance Imaging (MRI) . National Institute of Biomedical Imaging and Bioengineering. 2024. Available from: <https://www.nibib.nih.gov/science-education/science-topics/magnetic-resonance-imaging-mri>
2. CT Scan Versus MRI Versus X-Ray: What Type of Imaging Do I Need? . Hopkinsmedicine.org. 2022. Available from: <https://www.hopkinsmedicine.org/health/treatment-tests-and-therapies/ct-vs-mri-vs-xray>
3. Pai A, Shetty R, Hodis B, Chowdhury YS. Magnetic Resonance Imaging Physics . Nih.gov. StatPearls Publishing; 2023 . Available from: <https://www.ncbi.nlm.nih.gov/books/NBK564320/>
4. Carsten Stüber, Pitt D, Wang Y. Iron in Multiple Sclerosis and Its Noninvasive Imaging with Quantitative Susceptibility Mapping. International Journal of Molecular Sciences . 2016 Jan 14 ;17(1):100–0. Available from: <https://pubmed.ncbi.nlm.nih.gov/26784172/>
5. Wang J-Y, Zhuang Q-Q, Zhu L-B, Zhu H, Li T, Li R, et al. Meta-analysis of brain iron levels of Parkinson’s disease patients determined by postmortem and MRI measurements. Scientific Reports. 2016;6(1).
6. Carsten Stüber, Pitt D, Wang Y. Iron in Multiple Sclerosis and Its Noninvasive Imaging with Quantitative Susceptibility Mapping. International Journal of Molecular Sciences . 2016 Jan 14 ;17(1):100–0. Available from: <https://pubmed.ncbi.nlm.nih.gov/26784172/>
7. Duyn J. MR susceptibility imaging. Journal of magnetic resonance (San Diego, Calif 1997 : Print) . 2013 Apr 1 ;229:198–207. Available from: <https://www.sciencedirect.com/science/article/abs/pii/S1090780712003576>
8. Shmueli K. Quantitative Susceptibility Mapping. Advances in magnetic resonance technology and applications (Online) . 2020 Jan 1 ;819–38. Available from: <https://www.sciencedirect.com/science/article/abs/pii/B9780128170571000330>
9. Ashley Wilton Stewart, Simon Daniel Robinson, Kieran O’Brien, Jin J, Widhalm G, Hangel G, et al. QSMxT: Robust masking and artefact reduction for quantitative susceptibility mapping. Magnetic Resonance in Medicine . 2021 Oct 22 ;87(3):1289–300. Available from: <https://pubmed.ncbi.nlm.nih.gov/34687073/>
10. Acosta-Cabronero J, Betts M, Cardenas-Blanco A, Nestor PJ. In Vivo MRI Mapping of Brain Iron Deposition across the Adult Lifespan . ResearchGate. Society for Neuroscience; 2016 . Available from: [https://www.researchgate.net/publication/290481739\\_In\\_Vivo\\_MRI\\_Mapping\\_of\\_Brain\\_Iron\\_Deposition\\_across\\_the\\_Adult\\_Lifespan](https://www.researchgate.net/publication/290481739_In_Vivo_MRI_Mapping_of_Brain_Iron_Deposition_across_the_Adult_Lifespan)
11. Koch KM, Xenophon Papademetris, Rothman DL, Robin. Rapid calculations of susceptibility-induced magnetostatic field perturbations for *in vivo* magnetic resonance. Physics in Medicine and Biology . 2006 Nov 27 ;51(24):6381–402. Available from: <https://pubmed.ncbi.nlm.nih.gov/17148824/>
12. Quantitative susceptibility mapping: Report from the 2016 reconstruction challenge . Google.co.uk. 2016 . Available from: [https://scholar.google.co.uk/citations?view\\_op=view\\_citation&hl=en&user=Qo5PDKIAAAAJ&citation\\_for\\_view=Qo5PDKIAAAAJ:j3f4tGmQtD8C](https://scholar.google.co.uk/citations?view_op=view_citation&hl=en&user=Qo5PDKIAAAAJ&citation_for_view=Qo5PDKIAAAAJ:j3f4tGmQtD8C)
13. QSM Consensus Organization Committee, Bilgic B, Costagli M, Chan KS, Duyn J, Langkammer C, et al. Recommended Implementation of Quantitative Susceptibility Mapping for Clinical Research in The Brain: A Consensus of the ISMRM Electro-Magnetic Tissue Properties Study Group. ArXiv . 2023 ;arXiv:2307.02306v1. Available from: <https://www.ncbi.nlm.nih.gov/pmc/articles/PMC10350101/#S25>
14. Clinical Impact of Deep Learning Reconstruction in MRI . RadioGraphics. 2023 . Available from: <https://pubs.rsna.org/doi/abs/10.1148/rg.220133?journalCode=radiographics>
15. Aniket Pramanik, M. Bridget Zimmerman, Jacob M. Memory-Efficient Model-Based Deep Learning With Convergence and Robustness Guarantees. IEEE transactions on computational imaging . 2023 Jan 1 ;9:260–75. Available from: <https://ieeexplore.ieee.org/document/10059176>
16. Section V-C, Aniket Pramanik, M. Bridget Zimmerman, Jacob M. Memory-Efficient Model-Based Deep Learning With Convergence and Robustness Guarantees. IEEE transactions on computational imaging . 2023 Jan 1 ;9:260–75. Available from: <https://ieeexplore.ieee.org/document/10059176>

17. Section VI-C, Aniket Pramanik, M. Bridget Zimmerman, Jacob M. Memory-Efficient Model-Based Deep Learning With Convergence and Robustness Guarantees. IEEE transactions on computational imaging . 2023 Jan 1 ;9:260–75. Available from: <https://ieeexplore.ieee.org/document/10059176>
18. Section VI-D, Aniket Pramanik, M. Bridget Zimmerman, Jacob M. Memory-Efficient Model-Based Deep Learning With Convergence and Robustness Guarantees. IEEE transactions on computational imaging . 2023 Jan 1 ;9:260–75. Available from: <https://ieeexplore.ieee.org/document/10059176>
19. Section V-B, Aniket Pramanik, M. Bridget Zimmerman, Jacob M. Memory-Efficient Model-Based Deep Learning With Convergence and Robustness Guarantees. IEEE transactions on computational imaging . 2023 Jan 1 ;9:260–75. Available from: <https://ieeexplore.ieee.org/document/10059176>
20. DeVito Z, Ansel J, Constable W, Suo M, Zhang A, Hazelwood K. Using Python for Model Inference in Deep Learning . arXiv.org. 2021 . Available from: <https://arxiv.org/abs/2104.00254>
21. Linear Algebra for Everyone, Gilbert Strang . Mit.edu. 2020 . Available from: <https://math.mit.edu/~gs/everyone/>
22. Wikipedia Contributors. Conjugate transpose . Wikipedia. Wikimedia Foundation; 2024 . Available from: [https://en.wikipedia.org/wiki/Conjugate\\_transpose](https://en.wikipedia.org/wiki/Conjugate_transpose)
23. Jonathan Richard Shewchuk. An Introduction to the Conjugate Gradient Method Without the Agonizing Pain . 1994. Available from: <https://www.cs.cmu.edu/~quake-papers/painless-conjugate-gradient.pdf>
24. UCL RCAS Team. Myriad - UCL Research Computing Documentation . Ucl.ac.uk. 2022 . Available from: <https://www.rc.ucl.ac.uk/docs/Clusters/Myriad/>
25. Severance C, Dowd K. High Performance Computing Available from: <https://oer.uinsyahada.ac.id/files/original/dc064f6034dbfcca0f2abc1096af6342.pdf>
26. Rares Salomir, Denis, Chrit Tw Moonen. A fast calculation method for magnetic field inhomogeneity due to an arbitrary distribution of bulk susceptibility. Concepts in magnetic resonance Part B, Magnetic resonance engineering [Internet]. 2003 Jan 1 [cited 2024 Apr 5];19B(1):26–34. Available from: <https://onlinelibrary.wiley.com/doi/abs/10.1002/cmr.b.10083>
27. Google Colaboratory [Internet]. Google.com. 2019 [cited 2024 Apr 5]. Available from: [https://colab.research.google.com/drive/1VnMbVW7roOkY\\_wjpUXUxhNli3BHjwWJB](https://colab.research.google.com/drive/1VnMbVW7roOkY_wjpUXUxhNli3BHjwWJB)
28. Wei K, Liang J, Fu Y, 2022 K, Wei A, Aviles-Rivero J, et al. TFPnP: Tuning-free Plug-and-Play Proximal Algorithms with Applications to Inverse Imaging Problems. Journal of Machine Learning Research [Internet]. 2022 [cited 2024 Apr 5];23:1–48. Available from: <https://jmlr.csail.mit.edu/papers/volume23/20-1297/20-1297.pdf>
29. Jupin DM. Metabolite-albumin interactions in human biofluids studied by NMR. Ubnrunl [Internet]. 2014 [cited 2024 Apr 5]; Available from: <https://repository.ubn.ru.nl/handle/2066/126012>